PAPER

Structural phase transitions and magnetic and spectroscopic properties of the double perovskites Sr2Co1−xMgxTeO6 (x = 0.1, 0.2 and 0.5)

B. Orayech,*[a] L. Ortega-San-Martín,[b] I. Urcelay-Olabarria,[a,c] L. Lezama,[c,d] T. Rojo,[e] María I. Arriortua[f] and J. M. Igartua[g]

The structural and magnetic properties of a series of ordered double perovskites with the formula $Sr_2Co_{1-x}Mg_xTeO_6$ (x = 0.1, 0.2 and 0.5) are investigated by X-ray diffraction, low temperature neutron diffraction, electron paramagnetic resonance and magnetic susceptibility. The progressive substitution of the paramagnetic Co^{2+} high spin ion by the diamagnetic Mg^{2+}, of about the same size, induces changes in the room temperature crystal structure, from a distorted $P2_1/n$ phase for the undoped Sr_2CoTeO_6 oxide to the $I4/m$ of the end member (Sr_2MgTeO_6). These perovskites experience structural transitions on heating, the temperature at which the transitions occur being smaller as x increases. The novel approach of mode-crystallography is used for the analysis. All oxides show antiferromagnetic exchange interactions between Co^{2+} ions but the long range antiferromagnetic order is not achieved for the phase with x = 0.5. The low temperature neutron diffraction data have been evaluated using a full symmetry analysis. Results are consistent with an unquenched orbital contribution of a high spin Co^{2+} ion.

1. Introduction

Double perovskites of the general formula $A_2BB'O_6$ (with A typically being an alkaline earth, B a low oxidation state transition metal and B' a small and highly charged ion) in which the B and B' ions are completely ordered in the structure are still of great interest. The possibility of different degrees of cation order in these oxides allows for the development of different properties that arise from the coupling of spin, charge and orbital degrees of freedom of the transition metal ions. Oxides of this type have received much attention in recent years due to the observation of properties with high application potential such as the large magnetoresistance and room temperature half metallicity observed in Sr_2FeMoO_6 and related oxides,[1,2] high ionic conductivity in $Sr_2Mg_{1-x}Mn_xMoO_{6-\delta}$[3] or the coexistence of ferroelectricity and ferromagnetism (multiferroic behavior) in Bi_2NiMnO_6[4] and La_2NiMnO_6.[5] More recently, some double perovskites have even been used as host materials for light emitting Eu^{3+} phosphors with promising results,[6] demonstrating that the double perovskite structure still holds interesting properties if appropriate elements are introduced into the lattice.

The study of cobalt containing double perovskites with the formula $A_2CoB'O_6$ has gained interest in recent years. $Ba_2CoMo_{0.5}Nb_{0.5}O_{6-\delta}$, with a mixed Co^{2+}/Co^{3+} oxidation state, for example, was proposed as a potential Solid Oxide Fuel Cell (SOFC) cathode,[7] whereas $La_{2-x}Sr_xCoTiO_6$ oxides have shown promising results both as cathode and anode electrodes for SOFCs.[8] The oxides with the formula A_2CoTeO_6 (A = Sr, Pb, Ca, Ba and Cd) have shown, on the other hand, that their magnetic behavior does not follow the one observed in similar compounds with B' cations different from Te^{6+}.[9] The latter compounds show interesting structural changes when the A-site cation is changed (from conventional perovskite phases if A is small to hexagonal modifications if it is very large as in the case of Ba^{2+} ions[10]) and also when the temperature is changed (if A = Sr[11] or Pb,[12] so far). The latter compounds, despite the differences in their structure, always show antiferromagnetic behavior due to the super-exchange interactions between Co^{2+} ions.

[a]*Departamento de Física de la Materia Condensada, Facultad de Ciencia y Tecnología, Universidad del País Vasco, P.O. Box 644, Bilbao 48080, Spain. E-mail: brahim.orayech@ehu.es*
[b]*Departamento de Ciencias, Sección Química, Pontificia Universidad Católica del Perú (PUCP), Av. Universitaria 1801, Lima-32, Peru*
[c]*BCMaterials, Technological Park of Biscay, 48160 Derio, Spain*
[d]*Departamento de Química Inorgánica, Universidad del País Vasco, Apdo. 644, 48080 Bilbao, Spain*
[e]*CICenergigune, Albert Einstein 48, 01510 Miñano, Alava, Spain*
[f]*Universidad del País Vasco/Euskal Herriko Unibertsitatea (UPV/EHU). Facultad de Ciencia y Tecnología, Dpto. Mineralogía y Petrología, B. Sarriena s/n, 48940 Leioa (Vizcaya), Spain*
[g]*Fisika Aplikatua II Saila, Zientzia eta Teknologia Fakultatea, Euskal Herriko Unibertsitatea, P.O. Box 644, Bilbao 48080, Spain*

We present a rigorous study on the title solid solution: X-ray powder diffraction at low-, room- and high-temperature, neutron diffraction at low- and room-temperature for one of the new members, spectroscopic measurements, diffusive reflectance, EPR, DC magnetic susceptibility and magnetization experiment results will be presented and discussed.

We performed all the structural analyses using the mode-crystallography approach,[13–17,40] which is a perfect tool to analyze and study phase transitions, one of the main goals of the manuscript. The approach is based on the symmetry of a prototype phase, and its irreps, and on the natural breaking of that symmetry. The theoretical treatment is well known, but its implementation in crystallographic tools, its application and its systematic use in the refinements are very novel: we are re-visiting the pure Co material using this approach and the rest of the members of the solid solution are new. We have tried to make a comprehensive manuscript to give the theoretical clues, the practical steps and the more common tools and usage to refine and analyze the results in terms of symmetry-adapted modes. Using the jargon of mode-crystallography it is very easy and efficient to relate the distortions of the intermediate distorted phases. We are able to distinguish the degree of distortion; they are not only tilts of the octahedra: they are the only effective displacements of the atoms with respect to the high-symmetry phase. The new set of degrees of freedom (modes) is effectively and experimentally reduced, which facilitates the refinement and analysis.

We report one of the most common difficulties in refining these kinds of materials: the non-convergence of the refinement if one of the modes is not considered. With the usual set of degrees of freedom (the atomic coordinates), the refinement does not face any difficulty, because the atom coordinates are freed independently. Using modes, the gradation of the mode-amplitude values regarding some of them is dispensable, because their values are very very small, or their associated errors are very high. In this well known system, a double perovskite with a $P2_1/n$ space group, the underlying tri-linear coupling of the order parameters with a secondary one implies that even if the amplitude value for the tri-linearly coupled is very small, it is necessary to take it into account. We analyze the phase transitions in the framework of the Landau Theory of Phase Transitions, as we have the evolution of the actual order parameter. We have used and report the results from a rigorous, and not systematically used, method for obtaining the magnetic structure. We are re-visiting (in a very critical way and reporting a novel treatment) the pure Co case and correcting the way in which the magnetic structure was proposed.

2. Experimental

Polycrystalline $Sr_2Co_{1-x}Mg_xTeO_6$ with ($x = 0.1$, 0.2 and 0.5) were synthesized by the freeze-drying method. Stoichiometric quantities of $SrCO_3$, $Co(C_2H_3O_2)_2$, $Mg(C_2H_3O_2)_2$ and TeO_2 were dissolved in dilute aqueous nitric acid. The solutions were drop-by-drop frozen under liquid nitrogen. The frozen solutions were subsequently freeze-dried and the powders obtained were ground and calcined at 1170 K for 6 hours. The samples were ground, pelleted and calcined four times for 8 hours at 1270 K. Phase purity was confirmed by X-ray powder diffraction and the expected content of Sr, Co, Mg and Te in $Sr_2Co_{1-x}Mg_xTeO_6$ was verified by inductively coupled plasma atomic emission spectroscopy (ICP-AES) performed with an ARL Fisons 3410 spectrometer, see Table 1.

Neutron powder diffraction (NPD) experiments were carried out in the Institut Laue Langevin (ILL), Grenoble, France, on D2B and D1B instruments. For both experiments 6 g of a polycrystalline sample of $Sr_2Co_{0.9}Mg_{0.1}TeO_6$ were packed in an 8 mm diameter vanadium can, which was held inside a liquid helium cryostat. Data were collected at 4, 30 and 298 K on D2B using thermal neutrons of wavelength 1.594 Å in the angular range $5 \leq 2\theta \leq 162°$ in steps of 0.05° with an integration time of 50 000 monitor counts per step. Each point in the diffraction pattern was recorded by 6 independent detectors for subsequent normalization and summation, giving an overall collection time of approximately 3 hours for the entire data set. Temperature dependent NPD data were collected on D1B, using neutrons of wavelength 2.52 Å, every 2 K, from 2 to 34 K, over the angular range $10 \leq 2\theta \leq 90°$.

Room-temperature X-ray powder diffraction (XRPD) data were collected in the range $17 \leq 2\theta \leq 105°$ in steps of 0.02° with an integration time of 17 seconds per step using a Philips X'Pert MPD X-ray diffractometer with secondary beam graphite monochromatized Cu-Kα radiation. The room-temperature (RT) crystal-structure was refined simultaneously from X-ray and high-resolution neutron diffraction data. Temperature resolved XRPD data were collected using an Anton Påar HTK16 temperature chamber with a platinum stage mounted on the same diffractometer. The sample for high temperature measurement was mixed with acetone and a high temperature resin and applied to the Pt stage. To monitor the evolution of several characteristic peaks, data were collected every 10 K

Table 1 Compositional analysis of the $Sr_2Co_{1-x}Mg_xTeO_6$ ($x = 0.1$, 0.2 and 0.5) compounds

Compounds	x	0.1	0.2	0.5
Sr	% Calc.	38.6	38.9	39.8
	AAS	38.8(3)	—	39.1(3)
	ICP[a]	35(1)	38.1(1)	39(1)
Co	% Calc.	11.7	10.4	6.7
	AAS	11.2(1)	—	6.1(1)
	ICP[a]	10.9(1)	10.2(1)	6.0(2)
Te	% Calc.	28.1	28.3	29.0
	AAS	28.7(3)	—	27.9(1)
	ICP[a]	26.7(3)	25(1)	29(1)
Mg	% Calc.	0.53	1.08	2.76
	AAS	0.54(1)	—	2.70(2)
	ICP[a]	0.48(1)	0.96(1)	2.59(6)

[a] The wavelengths (in nm) used for the analysis were: $\lambda_{Sr} = 421.552$, $\lambda_{Co} = 238.89$, $\lambda_{Mg} = 279.553$ and $\lambda_{Te} = 214.281$.

from 300 to 870 K in the angular ranges $72 \leq 2\theta \leq 78°$ and $91 \leq 2\theta \leq 95°$. Higher quality, temperature-dependent XRPD data for subsequent Rietveld refinement were collected in the range $17 \leq 2\theta \leq 95°$ in steps of $0.05°$ with an integration time of 12 seconds per step, between 300 and 870 K, every 25 K.

Diffraction data were treated using the FullProf Suite program package[18] and Jana2006.[19] Magnetic structures were plotted using the Vesta program.[20]

Spectroscopic measurements were made by both diffuse reflectance and electron paramagnetic resonance. The diffuse reflectance spectra were recorded on a Cary 2415 spectrometer and registered at RT in the $5000–50\,000$ cm^{-1} range. X-Band EPR spectra were recorded between 0 and 7 kOe from 300 to 5 K on a Bruker ESP 300 spectrometer. The temperature was controlled using an Oxford Instruments (ITC4) regulator. The magnetic field was measured with a Bruker BNM 200 gaussmeter and the frequency inside the cavity was determined using a Hewlett-Packard 5352B microwave frequency counter.

DC magnetic susceptibility measurements were performed using a Quantum Design MPMS-7 SQUID magnetometer whilst heating from 5 to 300 K in an applied field of 1 kOe, after cooling either in the presence (field cooling, FC) or absence (zero field cooling, ZFC) of the applied field.

Magnetization as a function of applied field (H) was measured using the same MPMS-7 SQUID magnetometer at 5 K after cooling the sample in zero field. During the measurement, the field was swept between 70 and 270 kOe. Magnetization was also measured as a function of temperature between 5 and 40 K.

3. Results and discussion

3.1. Room-temperature crystal-structures

The room-temperature crystal structures of the polycrystalline samples of $Sr_2Co_{1-x}Mg_xTeO_6$ have been analyzed by using X-ray powder diffraction (XRPD), for all the compositions, and by using high resolution neutron powder diffraction (NPD) for one of them: $x = 0.1$.

Due to the high degree of pseudo-symmetry observed in double perovskites, the symmetry assignment was done observing the small reflections and the split ones,[21] which result from the distortion of the ideal prototype of cubic symmetry: $Fm\bar{3}m$ (no. 225, ITA).[22] $Sr_2Co_{0.9}Mg_{0.1}TeO_6$ was analyzed following the same protocol as with the parent phase ($x = 1$). All the observed reflections in the pattern of $Sr_2Co_{0.9}Mg_{0.1}TeO_6$ could be indexed in a cell with parameters $a \approx \sqrt{2}a_p$, $b \approx \sqrt{2}a_p$ and $c \approx 2a_p$.

The splitting of the cubic reflection $(444)_c$, Fig. 1, is very important to assign the symmetry; it was analyzed considering it as the triplet (404), (-404) and (044), which indicates that $a \neq b$ and $\beta \neq 90°$. This fact, together with the presence of the mentioned reflections, can be explained by a primitive cell and a monoclinic distortion, so the usual monoclinic space group was assigned to the RT crystal structure: $P2_1/n$ ($P12_1/n1$, non-standard setting of the $P2_1/c$, no. 14 space group).[22]
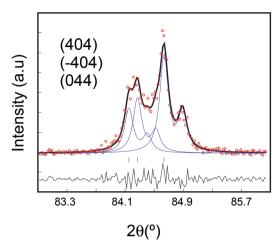

Fig. 1 Splitting of the singlet cubic reflection $(444)_c$ into a triplet: (404), (-404) and (044) reflections. The plot shows a fit with three reflections.

Fig. 2a shows that the $[(311)(-311),(131)(-131)]$ primitive doublet reflection disappears for $x = 0.2$ (for completeness, we are also showing the $x = 0$, 0.1, 0.2, 0.5 and 1 compositions in this figure). The two compositions $Sr_2Co_{1-x}Mg_xTeO_6$ with $x \geq 0.2$ analyzed in the present work could be indexed in an I centered cell, with the same metrics and with a splitting scheme compatible with a monoclinic symmetry, so we assigned the monoclinic space group $I2/m$ ($I12/m1$ non-standard setting of $I2/c$, no. 12 ITA) to the RT structures of those compositions. However, a new transformation can be suspected with the increase of x, as observed by the decrease of the splitting in some reflections (Fig. 2b and c).

In a recent report,[23] the authors show evidence proving that the RT space group of Sr_2MgTeO_6 is $I4/m$. We have also measured that composition and, in our case also, the high degree of pseudo-symmetry and the fact that we only have laboratory XRPD data have forced us to assign the tetragonal space group. In conclusion, in the progressive diminution of the monoclinic distortion, as the Mg doping increases, there should be an intermediate composition, $x > 0.5$, for which the monoclinic distortion disappears.

Rietveld refinement[18] of the crystal structures was performed using the program AMPLIMODES for FullProf,[24] part of the Bilbao Crystallographic Server,[25,26] and the WinPlotr/FullProf package.[27] The peak shape was described using a pseudo-Voigt function, and the background level was modeled using a polynomial function. The refined parameters were: scale factor, zero shift, lattice constants, peak profile, asymmetry parameters, amplitudes of the modes transforming according to the irreducible representations (irreps) and independent isotropic atomic displacement parameters. The high contrast between the Co and Te cations in the simultaneous refinements of the X-ray and neutron data allowed us to free their fractions: no disorder was found. Oxygen fractions were also freed, but the obtained values were so close to unity that they were fixed at 1.
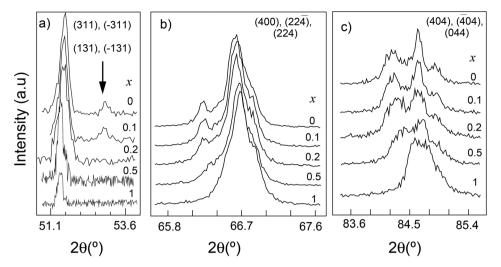
Fig. 2 Selected 2θ intervals for the four compositions of the $Sr_2Co_{1-x}Mg_xTeO_6$ series. (a) Disappearance of the reflection that violates the I-centering conditions on the *hkl*. (b, c) Change of the cubic reflection splitting with the increase of the magnesium content.

The initial structural information needed for the symmetry-adapted mode analysis with AMPLIMODES[15,24,28–33] is: the reference structure, a high symmetry phase (the prototype cubic phase for the ordered double perovskites, space group $Fm\bar{3}m$: atomic positions and cell-parameters); the RT phase's cell-parameters and space group ($P2_1/n$, for (x = 0.0, 0.1) compositions, and $I2/m$, for (x = 0.2, 0.5)); and finally, the transformation matrix between both cells: the reference and the RT cell.[28,29] A complete description of the procedure is given in ref. 29. For completeness of the refinements, we are including the x = 0.0 composition in all the calculations.

For the symmetry-mode analysis AMPLIMODES performs, it is not necessary to know a real prototype structure. The contributions of the much more important symmetry-breaking distortion-modes present in the distorted phase do not depend on any choice of the atomic coordinates of the prototype structure. To our knowledge, at the time of writing this report, there is no experimentally known cubic symmetry structure for these compounds. Hence, for the sake of simplicity of the comparisons, we have adopted the same high temperature high symmetry structure for all the compositions in this report and in future reports related to the same families. We expect to find the parent structure at high-temperatures, if no decomposition of the material takes place. AMPLIMODES obtains a complete basis of symmetry-adapted distortion modes and decomposes the distortion in terms of this basis of symmetry modes, and calculates the amplitudes for each of the symmetry adapted distortions. Modes are given in terms of atomic displacements in relative units for the atoms of the asymmetric unit of the distorted phase. The results of AMPLIMODES are shown in Table 2.

In the case of the RT monoclinic space group $P2_1/n$, there are seven irreducible representations (irreps) of the $Fm\bar{3}m$ space group that can take part in the symmetry breaking, and

these are as shown in Table 2: GM_1^+ (1) (totally symmetric), GM_3^+ (1), GM_4^+ (1), GM_5^+ (4), X_2^+ (1), X_3^+ (1) and X_5^+ (3). The theoretical predictions (and the Rietveld refinement of the mode amplitudes, see below) suggest that there is more than one active mode responsible for the $Fm\bar{3}m \rightarrow P2_1/n$ symmetry break: $P2_1/n$ phase cannot be generated by a single mechanism, or a single unstable mode of the cubic configuration. At least two modes must be present. These two active modes responsible for the stabilization of the $P2_1/n$ phase in double perovskites are known to be transforming according to the GM_4^+ and X_3^+ irreps.[29,30] On the other hand, there are five irreps of the $Fm\bar{3}m$ space group that can take part in the symmetry breaking from that space group to the room-temperature $I2/m$ monoclinic space group: GM_1^+, GM_3^+ (1), GM_4^+ (1) and GM_5^+ (2), twice.

It is worth noting that the output for the $Fm\bar{3}m \rightarrow I2/m$ symmetry breaking is contained in the $Fm\bar{3}m \rightarrow P2_1/n$ symmetry breaking. Nevertheless, for the former, as there are two irreps, *i.e.* GM_4^+ and GM_5^+, that break the symmetry down to $I2/m$, there are two possible primary order parameters. The final refinement results for the amplitude values of the modes involved in this symmetry break (see Fig. 5 in ref. 30) indicate that, from the two possible primary order parameters, there is only one, GM_4^+, whose amplitude is at least one order of magnitude greater than the rest of the amplitudes. The polarization vector associated with GM_4^+, going down to $P2_1/n$ or going down just to $I2/m$, is the same and it involves all the oxygen atoms in the monoclinic phases (three distinct in $P2_1/n$ and two distinct in $I2/m$). GM_4^+ is essentially a rotation of the octahedra around the *b* axis in the monoclinic cell; although it also slightly distorts the octahedra, the amount of rotation of the oxygens in the *ab* plane, ($\approx$0.25, $\approx$0.25, $\approx$0) set of coordinates, and the one above and perpendicular to that plane, ($\approx$0, $\approx$0, $\approx$0.25) set of coordinates, are not the same.

Table 2 Input information for AMPLIMODES for FullProf: high-symmetry phase information (prototype structure), low-symmetry structure information and transformation matrix for $Sr_2Co_{1-x}Mg_xTeO_6$. $P2_1/n$ (ITA no. 14, non-standard setting), $I2/m$ (ITA no. 12, non-standard setting), $I4/m$ (ITA no. 87, standard setting) and $Fm\bar{3}m$ (ITA no. 225, standard setting). The second part shows a list of the irreps taking part in the symmetry breaking from the cubic space group ($Fm\bar{3}m$) to the monoclinic $P2_1/n$ and $I2/m$ space groups observed experimentally at RT, and to the tetragonal space group $I4/m$, observed as an intermediate high-temperature space group. The list is part of the output of AMPLIMODES for FullProf. The number in parentheses indicates the number of modes transforming according to the irrep. The irreps in bold are the ones representing the order parameters: 2 in the $P2_1/n$ and one in the $I2/m$ space groups, respectively (see the text)

High-symmetry structure
225
7.9209 7.9209 7.9209 90.00 90.00 90.00
4

Te	1	4a	0.00000	0.00000	0.00000
M	1	4b	0.50000	0.50000	0.50000
Sr	1	8c	0.25000	0.25000	0.25000
O	1	24e	0.24714	0.00000	0.00000

Low-symmetry cell	Low-symmetry cell	Low-symmetry cell
014	012	087
5.5569 5.5932 7.8647 90.00 90.013 90.00	5.5574 5.5782 7.8506 90.00 90.06 90.00	5.6009 5.6009 7.9209 90.00 90.01 90.00
Transformation matrix	Transformation matrix	Transformation matrix
$\begin{pmatrix} 1/2 & 1/2 & 0 & 0 \\ -1/2 & 1/2 & 0 & 0 \\ 0 & 0 & 1 & 0 \end{pmatrix}$	$\begin{pmatrix} 1/2 & 1/2 & 0 & 0 \\ -1/2 & 1/2 & 0 & 0 \\ 0 & 0 & 1 & 0 \end{pmatrix}$	$\begin{pmatrix} 1/2 & 1/2 & 0 & 0 \\ -1/2 & 1/2 & 0 & 0 \\ 0 & 0 & 1 & 0 \end{pmatrix}$

Atoms	WP	Modes
$Fm\bar{3}m \rightarrow P2_1/n$		
O1	24e	GM_1^+ (1) GM_3^+ (1) **GM_4^+ (1)** GM_5^+ (2) X_2^+ (1) X_3^+ (1) X^{5+} (2)
Sr1	8c	GM_5^+ (2) X_5^+ (1)
$Fm\bar{3}m \rightarrow I2/m$		
O1	24e	GM_1^+ (1) GM_3^+ (1) **GM_4^+ (1)** GM_5^+ (2)
Sr1	8c	GM^{5+} (2)
$Fm\bar{3}m \rightarrow I4/m$		
O1	24e	GM_1^+ (1) GM_3^+ (1) **GM_4^+ (1)**

Table 3 Amplitudes of the modes (in Å) of the irreps taking part in the symmetry breaking from the $Fm\bar{3}m$ space group to the monoclinic space groups $P2_1/n$ and $I2/m$ for $Sr_2Co_{1-x}Mg_xTeO_6$ (x = 0.0, 0.1, 0.2, 0.5) compounds at room-temperature after the refinement of (a) all modes and (b) only the effectively acting mode-amplitudes

Irrep	Amplitude							
	Sr_2CoTeO_6		$Sr_2Co_{0.9}Mg_{0.1}TeO_6$		$Sr_2Co_{0.8}Mg_{0.2}TeO_6$		$Sr_2Co_{0.5}Mg_{0.5}TeO_6$	
	$P2_1/n$-NPD		$P2_1/n$-NPD		$I2/m$-XRPD		$I2/m$-XRPD	
	(a)	(b)	(a)	(b)	(a)	(b)	(a)	(b)
GM_1^+	0.1825(4)	0.1840(1)	0.1833(4)	0.1881(4)	0.0622(3)	0.0000	0.1102(3)	0.0000
GM_3^+	0.0173(2)	0.0000	0.0007(1)	0.0000	0.0943(1)	0.0000	0.0075(6)	0.0000
GM_4^+	0.7941(1)	0.7964(5)	0.7770(1)	0.7814(2)	0.5741(3)	0.6742(3)	0.6174(6)	0.6680(6)
GM_5^+	0.0230(1)	0.0000	0.0630(1)	0.0000	0.0765(5)	0.0000	0.0866(5)	0.0000
X_2^+	0.0074(5)	0.0000	0.0165(5)	0.0000				
X_3^+	0.2680(1)	0.2648(6)	0.1737(5)	0.1863(2)				
X_5^+	0.0032(2)	0.0037(1)	0.0469(5)	0.0263(4)				

Theory also states that those modes that experimentally should break the symmetry down to the RT observed phase should be the ones with the highest amplitudes. This is also observed experimentally as shown in Table 3: there are three global mode-amplitudes (GM_4^+, X_3^+ and X_5^+ irreps) that are higher than the rest. The necessary ones to break the symmetry are GM_4^+ and X_3^+, as these are the ones that have the RT monoclinic space group as the maximum subgroup.

Indeed, in the case of the primitive monoclinic RT space group symmetry $P2_1/n$, all modes, except for GM_4^+ and X_3^+, do appear as degrees of freedom due to the symmetry break. In the case of the $I2/m$ RT space group, the modes allowed by symmetry (but not breaking) are all modes except GM_4^+. For symmetry considerations, and referring to displacive phase-transitions, they represent allowed atomic displacements giving rise to configurations of higher symmetry than that of the low-symmetry space group and compatible with the parent space group of higher symmetry. The space groups of these (intermediate) configurations are the isotropy space groups. These compatible displacements are described by the amplitudes of the modes associated with the rest of the irreps: GM_3^+, GM_5^+ and X_2^+, in the primitive space group; and GM_3^+ and GM_5^+, in the centered space group. These amplitudes can have big (always smaller than the symmetry breaking ones) or small values. Indeed, if they have small values they can be fixed at zero without affecting the results and improve the efficiency of the refinement due to the use of less degrees of freedom.

Table 3 shows the final amplitude values, at RT, of the two different refinements performed on all the compositions, including the pure Co. In the first refinement we freed all the mode amplitudes and in the second one, only those fulfilling the above criteria: GM_4^+, X_3^+ and X_5^+ in $P2_1/n$ and GM_4^+ for $I2/m$. The resulting neutron powder diffraction (NPD) and X-ray powder diffraction (XRPD) patterns from the refinements of the four compounds at RT are shown in Fig. 3. Tables 4 and 5 show, respectively, the structures and the distances resulting from the two different refinements mentioned. The general conclusion regarding the set of amplitudes and the set of structures is the same: there is no appreciable difference between the model with all the freedom or with a (symmetry-guided-) restricted freedom. The fixed amplitudes left the atomic displacements related to the corresponding modes without effect, which indicates that the distortion with respect to the cubic prototype phase they represent is not effectively present.

Hence, some atomic coordinates in the RT distorted structure do not differ from those in the prototype cubic. This is the case, for instance, of the Sr cation, located in the 8c Wyckoff position (0.25 0.25 0.25) in the cubic prototype, which is (0.0 0.50 0.25) described in the $P2_1 = n$ cell: it moves to (0.0 0.4976 0.25). Only its y-coordinate has changed in the refinement.

Fig. 4a shows the mode-amplitudes *versus* the tolerance factor value (t). It is worth noting that the interval for the calculated (t) values is actually very small, 2.5×10^{-3}. Nevertheless, as expected from the previous analysis, there are two regions for the values of the GM_4^+ amplitude, corresponding to the two monoclinic space groups: the primitive and the centered. The $x = 0.0, 0.1$ compositions show the same value, and in the $x = 0.2, 0.5$ compositions, the same happens: both materials show the same distortion and both values are almost equal. Hence, we distinguish both distortions in the symmetry change. Of course, the octahedral tilt-angles in the centered phase are a little bit smaller than those in the primitive.

Regarding the evolution of the cell parameters and the volume of the unit cell (Fig. 4b), it can be said that the relative variation of the cell parameters (5%, for a–b, which is the biggest one) is three times smaller than the relative variation of the amplitudes: $\approx 15\%$.

3.2. High-temperature crystal-structures

Since $Sr_2Co_{0.9}Mg_{0.1}TeO_6$ is the only material with $P2_1/n$ symmetry at RT, the thermal study was focused initially on the reflections which do not satisfy the condition $h + k + l = 2n$ such as the $[(311)(-311),(131)(-131)]$ group (Fig. 5), which disappear between 300 and 400 K. The non-primitive reflections underwent no change at that temperature, so the patterns were fitted in the $I2/m$ space group.

Diffraction patterns in Fig. 6 show the thermal evolution of the splitting of the cubic reflection (444) for all the materials of the $Sr_2Co_{1-x}Mg_xTeO_6$ series. The group of reflections around $84°$ in 2θ lose completely their splitting at about 620 K, 620 K and 570 K, for $Sr_2Co_{0.9}Mg_{0.1}TeO_6$, $Sr_2Co_{0.8}Mg_{0.2}TeO_6$ and $Sr_2Co_{0.5}Mg_{0.5}TeO_6$, respectively, and consequently, all the reflections of the patterns can be fitted by a model based on the tetragonal space group $I4/m$ above the cited temperatures. At even higher temperatures, all the peaks become unique, as seen in Fig. 6. This indicates that the materials undergo a final structural transition from the tetragonal structure to the parent phase, cubic. This transition occurs at lower temperatures with the increase of x.

In the tetragonal-($I4/m$)-to-cubic ($Fm\bar{3}m$) phase-transition there are two mono-dimensional modes (the third irrep, GM_1^+ is the totally symmetric), GM_3^+ (1) and GM_4^+ (1), all of them involving oxygen atoms located at the 24e Wyckoff positions of the prototype cubic phase. The GM_3^+ mode is responsible for the breaking of the symmetry to the $I4/mmm$ tetragonal space group. This mode involves the movement of all the oxygen atoms in the octahedra in such a way that the oxygens located in the (00z) positions move to the center of the octahedra; the oxygen atoms located in the xy plane move outwards along the diagonals of the basal plane of the octahedra. On the other hand, the mode GM_4^+ is responsible for the breaking of the symmetry down to the $I4/m$ space group, and involves movements only of the oxygens located in the xy plane.

It is worth noting that despite the fact that the irreps of the primary modes lowering successively the symmetry from the cubic to the monoclinic space groups ($I2/m$) are the same, in both cases involve only oxygen atoms, and can be interpreted as tilts of the octahedra; the cubic-to-tetragonal phase transition is continuous, as predicted by theory, and the tetragonal-to-monoclinic is discontinuous. The discontinuous character of the last transition is related to the change in the direction of the GM_4^+ irrep on the three-dimensional representation space.[30] The direction of the GM_4^+ irrep in the $I4/m$ phase is $(0,0,a)$, while it changes to $(a,a,0)$ in the monoclinic phases. From a structural point of view, this change in the direction is reflected on the relative orientation of both space groups: $I2/m$ is a subgroup of $I4/m$, but when the two-fold axis is located in the same direction as the four-fold one, which is
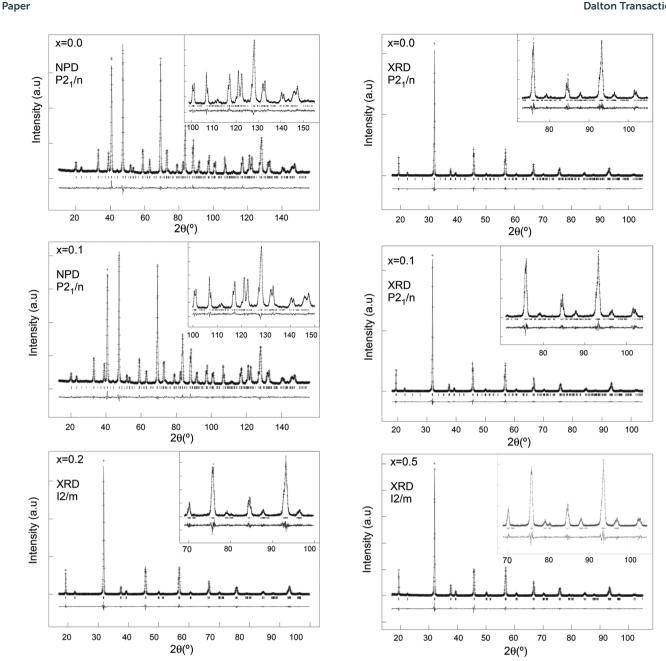
Fig. 3 Experimental (symbols) and calculated (line) X-ray profiles and neutron profiles for the Rietveld refinement of the $Sr_2Co_{1-x}Mg_xTeO_6$ series at room temperature using a structural model with the $P2_1/n$ space group for ($x = 0.0$ and 0.1) and $I2/m$ for ($x = 0.2$ and 0.5). The bars in the lower part of the graphics represent the Bragg peak positions.

not the case. There is no way to go in a continuous manner from the tetragonal to the monoclinic symmetry when the two-fold axis is perpendicular to the four-fold axis, as is the case in the tetragonal-to-monoclinic phase transition.

Fig. 7 shows the temperature evolution of the mode-amplitudes set free in the final restricted refinement and the cell parameters. First of all we would like to stress that we have found experimentally the cubic prototype phase. As mentioned, the transition from the cubic to the intermediate distorted tetragonal phase is continuous, as observed in Fig. 7.

On the other hand, the finite jump at the same transition in the amplitude values could be attributed to the non-complete second order character of the transition. This is often observed experimentally in these kinds of systems. In the framework of the Landau Theory of Phase Transitions[34] the jump can be explained by including in the expansion of the free energy a sixth-order term in the order parameter, in the case when the fourth order term is not enough to stabilize the symmetry break caused by the sign change of the second-order term, or in the case when the fourth order term is

Table 4 Crystal structure data and refinement results for $Sr_2Co_{1-x}Mg_xTeO_6$ (x = 0.0, 0.1, 0.2 and 0.5) from NPD at room-temperature after the refinement of (a) all modes and (b) only the effectively acting mode. Co/Mg (2b (0,0,1/2)), Te (2a (0,0,0))

		Sr_2CoTeO_6 $P2_1/n$-NPD		$Sr_2Co_{0.9}Mg_{0.1}TeO_6$ $P2_1/n$-NPD		$Sr_2Co_{0.8}Mg_{0.2}TeO_6$ $I2/m$-XRPD		$Sr_2Co_{0.5}Mg_{0.5}TeO_6$ $I2/m$-XRPD	
		(a)	(b)	(a)	(b)	(a)	(b)	(a)	(b)
t		0.9758		0.9763		0.9769		0.9787	
Sr	x	−0.0003(4)	0.0000	−0.0015(4)	0.0000	0.001(3)	0.0000	0.006(5)	0.00000
	y	0.5003(1)	0.5003(1)	0.4970(1)	0.4976(1)	1/2	1/2	1/2	1/2
	z	0.2492(7)	0.2500	0.2521(1)	0.2500	−0.7533(7)	−0.75000	−0.7553(12)	−0.75000
	B_{iso} (Å^2)	1.02(3)	1.03(1)	1.03(2)	1.07(2)	0.94(2)	0.94(2)	0.97(3)	0.97(3)
O1	x	−0.7460(7)	−0.7477(3)	−0.7721(1)	−0.7680(3)	0.223(4)	0.24714	0.235(6)	0.24714
	y	0.2285(7)	0.2286(3)	0.2536(1)	0.2486(3)	0.271(4)	0.24714	0.271(6)	0.24714
	z	−0.0238(1)	−0.0251(1)	−0.0271(1)	−0.0247(1)	−0.023(4)	−0.0301(1)	−0.017(7)	−0.0300(2)
	B_{iso} (Å^2)	1.06(1)	1.06(3)	1.32(1)	1.32(1)	1.06	1.06	1.06	1.06
O2	x	−0.4503(3)	−0.4497(2)	−0.4533(4)	−0.4533(2)	0.057(7)	0.060(2)	0.075(1)	0.060(4)
	y	0.5008(1)	0.5008(1)	0.4973(1)	0.4984(2)	0	0.00000	0	0
	z	−0.2604(5)	−0.2595(2)	−0.2596(5)	−0.2597(1)	−0.743(4)	−0.7528	−0.748(6)	−0.75286
	B_{iso} (Å^2)	1.06(1)	1.06(3)	1.32(1)	1.32(1)	1.06	1.06	1.06	1.06
O3	x	−0.2294(7)	−0.2286(3)	−0.2437(1)	−0.2486(3)				
	y	0.2518(7)	0.2523(3)	0.2359(1)	0.2320(3)				
	z	0.0267(1)	0.0251(8)	0.0242(1)	0.0246(1)				
	B_{iso} (Å^2)	1.06(1)	1.06(3)	1.32(2)	1.32(2)				
Te	B_{iso} (Å^2)	0.76(2)	0.77(3)	0.74(3)	0.79(3)	1.62(2)	1.62(2)	1.56(1)	1.56(1)
Co/Mg	B_{iso} (Å^2)	0.76(2)	0.77(3)	0.74(3)	0.79(3)	1.62(2)	1.62(2)	1.56(1)	1.56(1)
a (Å)		5.6434(1)	5.6434(1)	5.6417(1)	5.6417(1)	5.6302(4)	5.6304(3)	5.6230(1)	5.6230(1)
b (Å)		5.6091(1)	5.6091(1)	5.6074(1)	5.6074(1)	5.5986(4)	5.5988(4)	5.5968(1)	5.5968(1)
c (Å)		7.9271(2)	7.9270(2)	7.9213(1)	7.9213(1)	7.9078(5)	7.9078(5)	7.9060(1)	7.9060(1)
β (°)		89.950(4)	89.950(1)	89.952(4)	89.950(4)	89.985(6)	89.985(6)	89.985(1)	89.985(1)
V (Å^3)		250.92(1)	250.92(1)	250.93(1)	250.93(1)	249.28(3)	249.28(2)	248.83(1)	248.83(1)
R_p (%)		4.07	4.08	4.11	4.48	8.5	8.9	7.6	8.02
R_{wp} (%)		5.23	5.25	5.31	5.80	7.5	7.9	6.2	7.1
R_{exp} (%)		1.72	1.72	2.17	1.66	5.66	5.68	4.82	4.83
χ^2		6.25	6.31	5.98	6.06	6.57	6.93	11.3	11.2
R_{Bragg}		4.31	4.97	7.31	4.48	8.90	8.97	4.97	4.54

negative. Under these conditions, the sixth term forces the character of the phase transition to be of the first order. Apart from this, the evolution of the amplitudes as the external field is released (temperature is decreased) is the expected one: a continuous increase of the distortion. There are no appreciable jumps in the amplitude values evolution of GM_4^+ when the systems cross the phase transitions, down to the lowest temperatures measured, as expected. Finally, we remark on the relative values of the mode-amplitudes in $P2_1/n$. X_5^+ is almost 20 times smaller than the biggest one, in the three cases. It could be thought that only this fact would force us to take it out from the symmetry-directed refinement: this is the main argument on which our refinement process is based. Nevertheless, this mode has to be included in the refinement even if its values are so small. The reason is that it is trilinearly coupled[35] to the two order parameters and the non-inclusion in the refinement makes it non-converging. This is the behavior observed experimentally in these kinds of materials.

3.3. Spectroscopic measurements

Diffuse reflectance spectra of the $Sr_2Co_{1-x}Mg_xTeO_6$ compositions with x = 0.1, 0.2, and 0.5 are shown in Fig. 8, together with the data from the undoped sample, Sr_2CoTeO_6, for comparison.

In all cases, the characteristic bands of Co^{2+} (d^7) in a high spin octahedral coordination environment are observed. These bands correspond to the three allowed spin transitions of the Co^{2+} ions from the fundamental state $^4T_{1g}$ (^4F) to the excited states: $^4T_{2g}$ (^4F), $^4A_{2g}$ (^4F) and $^4T_{1g}$ (^4P).[11] The assignment of these bands, based on the energy diagrams of Tanabe–Sugano[36] of the Co^{2+} ion, is shown in Table 6, together with the crystal-field splitting parameter D_q and the Racah parameter, B.

One of the most significant aspects of these results is the reduction by 15% in the Racah parameter value B with respect to the free ion, which is 971 cm^{-1}. This reduction is traditionally interpreted in terms of the covalency contribution to the

Table 5 Main bond distances (Å) and selected angles (°) for $Sr_2Co_{1-x}Mg_xTeO_6$ (x = 0.0, 0.1, 0.2 and 0.5) at room temperature. The values were obtained refining (a) all modes and (b) only the effectively acting mode

	Sr_2CoTeO_6		$Sr_2Co_{0.9}Mg_{0.1}TeO_6$		$Sr_2Co_{0.8}Mg_{0.2}TeO_6$		$Sr_2Co_{0.5}Mg_{0.5}TeO_6$	
	$P2_1/n$-NPD		$P2_1/n$-NPD		$I2/m$-XRPD		$I2/m$-XRPD	
	(a)	(b)	(a)	(b)	(a)	(b)	(a)	(b)
Co/MgO₆ octahedra								
Co/Mg–O1	2.069(3) × 2	2.076(3) × 2	2.067(3) × 2	2.076(3) × 2	2.027(1) × 4	2.021(1) × 4	2.020(1) × 4	2.018(1) × 4
Co/Mg–O2	2.083(1) × 2	2.077(1) × 2	2.073(4) × 2	2.075(4) × 2	2.030(2) × 2	2.027(2) × 2	2.029(2) × 2	2.029(2) × 2
Co/Mg–O3	2.077(3) × 2	2.078(3) × 2	2.081(3) × 2	2.074(3) × 2				
Average distance	2.076(1)	2.077(1)	2.074(1)	2.075(1)	2.026(3)	2.023(3)	2.023(6)	2.022(6)
Predicted distance	2.0985	2.0985	2.0985	2.0985	2.0985	2.0985	2.0985	2.0985
TeO₆ octahedra								
Te–O1	1.932(3) × 2	1.926(3) × 2	1.927(3) × 2	1.921(3) × 2	1.977(1) × 4	1.976(1) × 4	1.975(1) × 4	1.973(1) × 4
Te–O2	1.920(1) × 2	1.927(1) × 2	1.922(3) × 2	1.923(3) × 2	1.986(2) × 2	1.983(2) × 2	1.985(2) × 2	1.985(2) × 2
Te–O3	1.927(3) × 2	1.925(3) × 2	1.919(4) × 2	1.922(4) × 2				
Average distance	1.926(1)	1.926(1)	1.923(1)	1.922(1)	1.981(6)	1.979(6)	1.978(6)	1.977(6)
Predicted distance	1.9170	1.9170	1.9170	1.9170	1.9170	1.9170	1.9170	1.9170
∠O1–Co/Mg–O2	89.9(4)	89.8(2)	89.8(4)	90.0(2)	89.9(1)	89.9(2)	89.9(2)	89.9(2)
∠O1–Co/Mg–O3	89.5(3)	89.1(1)	88.1(3)	89.1(1)	90.1(1) × 2	90.1(2) × 2	90.0(7) × 2	90.0(7) × 2
∠O2–Co/Mg–O3	89.8(3)	89.7(2)	89.2(4)	90.0(2)				
∠O1–Te–O2	89.4(4)	89.6(2)	89.8(4)	89.9(2)	89.9(3)	89.9(1)	89.9(4)	89.9(4)
∠O1–Te–O3	88.7(3)	89.1(1)	89.9(4)	89.1(1)	90.2(2) × 2	90.2(1) × 2	90.1(4) × 2	90.1(4) × 2
∠O2–Te–O3	89.5(4)	89.9(2)	89.0(4)	89.9(2)				
∠Co/Mg–O1–Te	166.8(2)	167.3(7)	168.6(2)	168.2(1)	165.6(5)	165.4(2)	165.7(5)	165.7(5)
∠Co/Mg–O2–Te	163.8(2)	163.7(5)	164.6(2)	164.1(1)	159.6(2) × 2	159.4(2) × 2	159.6(8) × 2	159.6(8) × 2
∠Co/Mg–O3–Te	167.7(2)	167.3(7)	167.0(2)	167.1(1)				

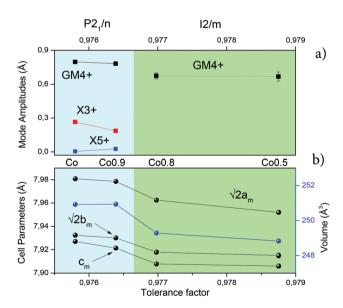**Fig. 4** Variation, as a function of the tolerance factor, of the three distortion irrep amplitudes GM₄⁺ (black), X₃⁺ (red) and X₅⁺ (blue), and the cell parameters (black) and the unit cell volume (blue) for the $Sr_2Co_{1-x}Mg_xTeO_6$ series at room-temperature. The colored backgrounds indicate the regions of the two space groups, $P2_1/n$ and $I2/m$, observed for the four compositions.

Fig. 5 Disappearance, as temperature increases, of the primitive reflections (311), (−311), (131) and (−131) of the $Sr_2Co_{0.9}Mg_{0.1}TeO_6$ compound.

crystal-field model (which is an electrostatic model) that can be applied to the Co–O bond. The lower B observed in these c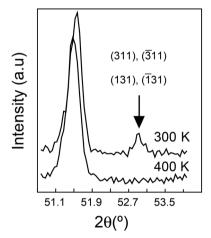ompounds compared to those in the table may be related to the high polarizing power of Te^{6+} ions. These ions withdraw much of the electron density of the oxide ions allowing a better delocalization of the d-electrons in the Co–O bond. This delocalization or nephelauxetic effect is the cause of the reduced B. Experimentally, it is common to observe Racah parameters in the range $0.7B_{free} < B < 0.9B_{free}$,[11] as is observed in the table, even if the covalency of the bond is not very high, as expected in these cases. It was previously shown that the degree of covalency of the Co(II)–O bond in similar perovskites
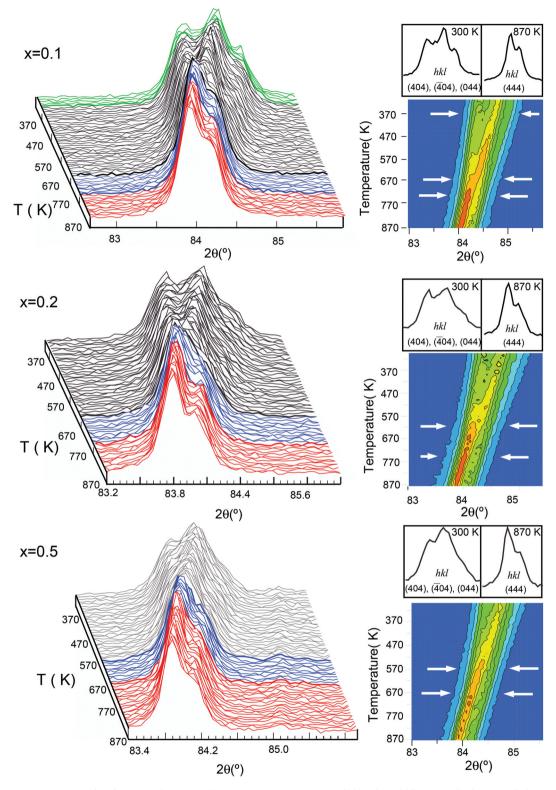
Fig. 6 Thermal evolution of the (444) cubic reflection splitting located in the interval (82° < 2θ < 86°) for the $Sr_2Co_{1-x}Mg_xTeO_6$ compounds with (x = 0.1, 0.2, 0.5). The splitting of the triplet (404), (−404) and (044) is clearly seen at 300 K, and as the temperature increases, the reflections get closer, up to 870 K where they remain as a single peak.
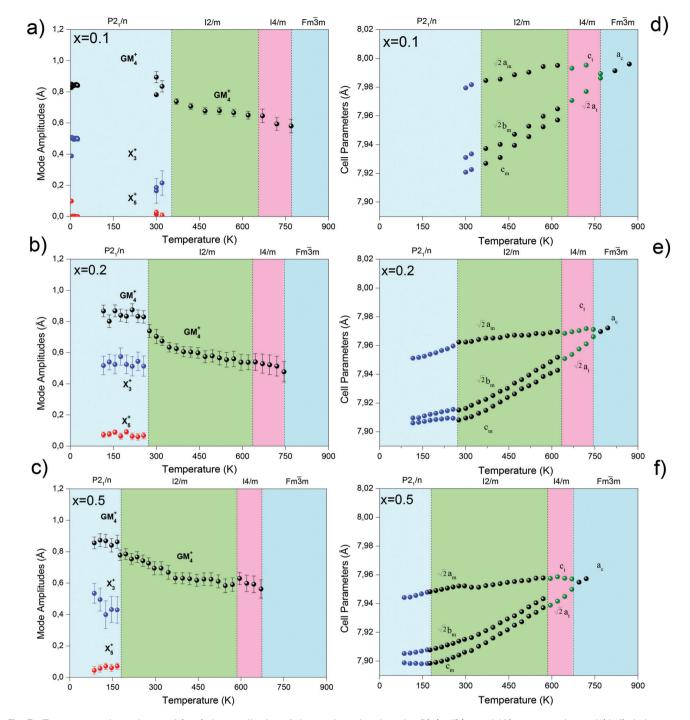
Fig. 7 Temperature dependence of (a–c) the amplitudes of the modes related to the $P2_1/n$, $I2/m$ and $I4/m$ symmetries and (d–f) their corresponding cell parameters, as obtained from NPD and XRD data refinements, for the $Sr_2Co_{1-x}Mg_xTeO_6$ compounds with (x = 0.0, 0.1, 0.2, 0.5).

was not very different from that of Co(II)-doped MgO. The fact that all bands appear mostly unchanged indicates that the cobalt environment in the compounds remains almost unchanged in the series, as observed from diffraction data.

3.4. EPR spectroscopy

X-band EPR spectra were recorded at different temperatures between 4 and 298 K for Sr_2CoTeO_6 [11] and $Sr_2Co_{0.5}Mg_{0.5}TeO_6$.

The high relaxation times and strong dipolar interaction characteristics of Co^{2+} ions focused the study on low temperatures, as no signal appears at RT. At 4 K, see Fig. 9a, the pure Sr_2CoTeO_6 showed no signal, which is usually common in a long range antiferromagnetically ordered compound, while the $Sr_2Co_{0.5}Mg_{0.5}$-TeO_6 phase showed a signal centered at a g value close to 4.5.

This signal is typical of a Co^{2+} ion in a more diluted environment in which cobalt ions are sufficiently separated

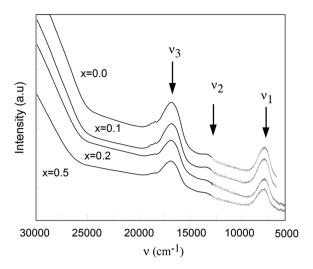**Fig. 8** Diffuse reflectance spectra of the $Sr_2Co_{1-x}Mg_xTeO_6$ (x = 0.0, 0.1, 0.2, 0.5) series, in the energy range of 5000–30 000 cm^{-1}.

from each other such that the dipolar and magnetic interactions do not perturb the hyperfine splitting. Fig. 9b shows an amplification of that signal. Although poorly resolved, it can be described in terms of an effective doublet spin 1/2 that interacts with the nuclear spin I = 7/2 of the ^{59}Co, as was already explained in the Co^{2+} doped Sr_2CoTeO_6.[11] The temperature evolution of the signal showed that it is superimposed on a stronger one, also centered at g = 4.5, with a width extending to the entire spectrum (insets in Fig. 9b). Since there is no evidence in the patterns of a possible impurity, the origin of the mixing of both signals has been attributed to an inhomogeneous distribution of Co and Mg in the phase, and this, in turn, precluded a rigorous analysis of the spectrum and its evolution with temperature.

3.5. Magnetic properties

The magnetic susceptibility measurements have been carried out between 5 and 300 K for all the compositions, with an applied field of 1 kOe. Fig. 10a–d show the variation of the molar magnetic susceptibility (χ_m), its inverse ($1/\chi_m$) and the product $\chi_m \cdot T$ as a function of temperature for all compositions.

The magnetic behaviors of all the compositions are very similar. At high temperatures, in the paramagnetic zone, the evolution of the inverse susceptibility with the temperature could be fitted to the classical Curie–Weiss law: $\chi = \dfrac{C_m}{(T - \theta)}$. Table 7 shows the obtained C_m and θ parameters. The obtained θ values (negative) and the descending trend of the curves ($\chi_m T$) $vs.$ T indicate that the main magnetic interactions are antiferromagnetic and, also, the spin–orbit coupling typical of the Co^{2+} in octahedral coordination.

Replacing the Co^{2+} ion (S = 3/2) with the Mg^{2+} ion (S = 0) causes a weakening of the antiferromagnetic interactions, as is clearly seen in the data shown in Table 7. Both the Curie–Weiss temperature, θ, and the ordering temperature (Néel temperature), T_N, decrease as the amount of Mg^{2+} increases. This indicates that, despite their different ionic sizes, Mg^{2+} is replacing cobalt ions randomly and homogeneously in all compounds. The possible presence of inhomogeneities, suggested in the EPR data of the x = 0.5 phase, could not be detected in the present data. The high degree of cobalt dilution prevents the onset of antiferromagnetic interactions in this case, although they are inferred by the sign of θ. Despite this, no signs of Co-clusterization are evident but this does not rule out their presence given that EPR spectroscopy is a more sensitive technique to local environment whereas magnetic susceptibility data are dominated by average behavior.

Table 7 includes the experimental effective magnetic moment values, μ_{eff}, observed in the $Sr_2Co_{1-x}Mg_xTeO_6$ series.
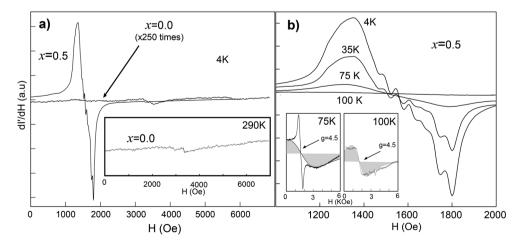

Fig. 9 (a) EPR spectra, at 4 K, for the oxides with x = 0.0, 0.5; in the inset, we have included the spectra of the former at room temperature. (b) Thermal evolution of the main EPR signal of the x = 0.5 composition. In the inset, we include two fitting results simulating the second signal of cobalt, observed in this composition.

Table 6 Experimentally observed band sets and the D_q and B parameters for the $Sr_2Co_{1-x}Mg_xTeO_6$ ($x = 0.0, 0.1, 0.2, 0.5$) series

x	ν_1 (cm^{-1})	ν_2 (cm^{-1})	ν_3 (cm^{-1})	D_q (cm^{-1})	B (cm^{-1})
0	6450	13 200	17 200	675	820
0.1	6450	13 300	17 200	675	820
0.2	6450	13 300	17 275	685	815
0.5	6450	13 300	17 275	685	815
$Co(H_2O)_6^{2+}$	8100	16 000	19 400	790	906
Co : MgO	8500	17 200	19 600	870	873

ν_1; $^4T_{1g}(^4F) \rightarrow {}^4T_{2g}(^4F)$; $5D_q - 7.5B + 0.5\sqrt{225B^2 + 100D_q^2 + 180D_qB}$.

ν_2; $^4T_{1g}(^4F) \rightarrow {}^4A_{2g}(^4F)$; $15D_q - 7.5B + 0.5\sqrt{225B^2 + 100D_q^2 + 180D_qB}$.

ν_3; $^4T_{1g}(^4F) \rightarrow {}^4T_{1g}(^4P)$; $\sqrt{225B^2 + 100D_q^2 + 180D_qB}$.

The obtained values are in very good agreement with the theoretical value of $5.20\mu_B$ expected for a system formed by the Co^{2+} cation with high-spin ($S = 3/2$) subjected to an unquenched orbital contribution to the magnetic moment ($L = 3$).

Fig. 11 shows the ZFC and FC magnetic susceptibility curves. There is a small irreversibility in the curves that could be caused by a misalignment or canting in the tridimensional magnetic order of the Co^{2+} spins, or could be caused by a spin glass-behavior due to the competition between ferromagnetic and anti-ferromagnetic interactions within the sample. However, the irreversibility is very small in magnitude, suggesting that the antiferromagnetic coupling of the Co^{2+} spins is very effective. In order to study the irreversibility, the remanent magnetization of the sample was measured as the temperature decreased down to 5 K under 100 Oe magnetic field. The obtained data are plotted in Fig. 12. At 5 K the residual magnetization is about 0.08 emu mol^{-1}, which reveals that the canting is very small.

3.6. Magnetic structure

The magnetic structures of Sr_2CoTeO_6 and $Sr_2Co_{0.9}Mg_{0.1}TeO_6$ have been determined using neutron powder diffraction data collected on D1B. In order to solve the spin arrangement, first the crystal structure has been refined from data collected on the high-resolution diffractometer D2B at 4 K. The diffraction patterns of both compounds show several new reflections which arise due to the long-range magnetic order of the Co^{2+} cations. These additional peaks were added to the refinements as a second phase. The collected data show no evidence of any structural phase transition at low temperatures and Rietveld refinements were carried out using the model previously deduced at RT ($P2_1/n$). Refined structural parameters are shown in Table 8. The only particularity is the diminution of the angles M–O–Te (M = Co, Mg), attributed to the slight monoclinic distortion, a consequence of the cell contraction caused by temperature.

Additional diffraction patterns (Fig. 13) have been collected on D1B as the temperature decreased. The magnetic reflections have been indexed with $\mathbf{k} = (0,0,0)$ propagation vector. In other words, the magnetic cell is equivalent to the crystalline

cell. The temperature at which magnetic peaks appear (16 K) reasonably coincides with that expected from magnetic susceptibility measurements in both cases.

The full symmetry of a paramagnetic state has an additional symmetry operation that has not been considered up to now: the time reversal {1′|000}. This operation leaves invariant all the atomic parameters of the atoms and reverses their magnetic moment. In these materials, the full symmetry of the crystal in the paramagnetic state is described by the Shubnikov group $P2_1/n1'$.[37] The magnetic ordering is a symmetry breaking process from a paramagnetic phase to a magnetically ordered one where the time-reversal symmetry is lost and, therefore, the symmetry of the emerging magnetic structure is described by a subgroup of $P2_1/n1'$ where the operation {1′|000} is not present.[37,38]

There are four maximal subgroups of $P2_1/n1'$ compatible with $\mathbf{k} = (0,0,0)$: $P2_1/n$, $P2'_1/n'$, $P2_1/n'$ and $P2'_1/n$. These subgroups have a one-to-one correspondence to the four magnetic irreps mG_1^+, mG_2^+, mG_1^- and mG_2^-, since the latter four are one-dimensional.[39] Being M_x, M_y and M_z the magnetic-moment components of an atom, each symmetry operation transforms them according to an axial vector and, if the symmetry operation includes the time reversal, an additional change of sign must be done to the moments. The $P2_1/n'$ and $P2'_1/n$ magnetic space groups forbid any magnetic ordering when the magnetic atom is located at the (0,0,1/2) position: these groups contain the {$\bar{1}$|000} operation that prohibits any magnetic ordering at that position and, therefore, these groups are discarded. In the case of $P2_1/n$ and $P2'_1/n'$, the three magnetic components of the Co atoms at the (0,0,1/2) position are independent (M_x, M_y, M_z). Once these components are determined, the orientation of the magnetic moments of the symmetry-related Co atom at the (1/2, 1/2, 0) position is fully determined: $(-M_x, M_y, -M_z)$ in $P2_1/n$, i.e. antiferromagnetic coupling for x- and z-spin components and ferromagnetic coupling for the y-spin component; and $(M_x, -M_y, M_z)$ in $P2'_1/n'$, antiferromagnetic coupling for the y-spin components and ferromagnetic coupling for x- and z-spin components.

Neutron diffraction data in the magnetically ordered phase of the pure Sr_2CoTeO_6 and the $Sr_2Co_{0.9}Mg_{0.1}TeO_6$ samples
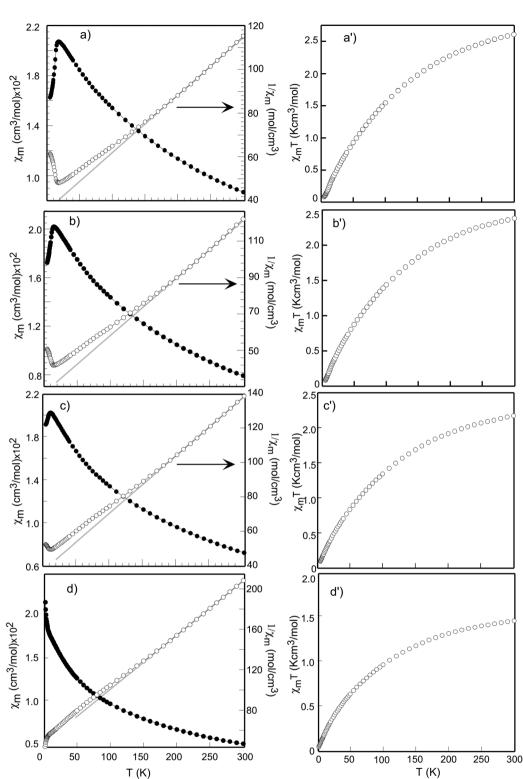
Fig. 10 (a–d) Susceptibility and its inverse curves for the (x = 0.0, 0.1, 0.2, 0.5) series. In grey, the Curie–Weiss law. (a'–d') Thermal evolution for the ($\chi_m \cdot T$) product, in the same series.

have been analyzed using both $P2_1/n$ and $P2'_1/n'$ magnetic space groups. It has been observed that for both compositions the data are best fitted using the space group $P2_1/n$, see

Fig. 14. The refined components of the magnetic structures are given in Table 9. According to the refinements, the y-spin component, that would give rise to macroscopic ferromagnetic

Table 7 Magnetic parameters for $Sr_2Co_{1-x}Mg_xTeO_6$, (0.1, 0.2 and 0.5) oxides obtained by dc-susceptibility (^{dc}), heat-capacity (^{hc}) and neutron-diffraction (nd) measurements. The table includes the parameters of the pure Sr_2CoTeO_6 for completeness taken from ref. 11

x	0	0.1	0.2	0.5
T_N^{dc} (K)	18	15	13	—
T_N^{hc} (K)	19	—	—	—
T_N^{nd} (K)	15	13	—	—
θ^{dc} (K)	−140	−125	−113	−88
C_m^{dc} (cm^3 K mol^{-1})	3.82	3.38	3.00	1.87
μ_{eff}^{dc} (μ_B)	5.53	5.20	4.90	3.87
μ_{eff}^{nd} (μ_B)	2.10	1.96	—	—

Fig. 12 Remanent magnetization as a function of the temperature for Sr_2CoTeO_6.

Fig. 11 FC and ZFC magnetic susceptibility curves in the $Sr_2Co_{1-x}Mg_xTeO_6$ (x = 0.0, 0.1, 0.2) series.

Table 8 Crystal structural data for $Sr_2Co_{1-x}Mg_xTeO_6$ (x = 0.0 and 0.1) at 4 K. The refinements have been done freeing only the mode-amplitude (see the text): GM_4^+, X_3^+ and X_5^+. The Co, Mg and Te cations are located in: Co/Mg [2b (0,0,1/2)], Te [2a (0,0,0)]

		Sr_2CoTeO_6	$Sr_2Co_{0.9}Mg_{0.1}TeO_6$
Sr	X	0.0000	0.0000
	Y	0.4911(4)	0.4922(5)
	Z	0.2500	0.2500
	B_{iso} (Å^2)	0.76(2)	0.86(2)
O1	x	−0.7798(2)	−0.7771(3)
	y	0.2592(2)	0.2579(3)
	z	−0.0267(1)	−0.0261(1)
	B_{iso} (Å^2)	0.95(2)	1.08(14)
O2	x	−0.44656(2)	−0.4477(2)
	y	0.5000	0.5000
	z	−0.26031(6)	−0.2595(2)
	B_{iso} (Å^2)	0.95(1)	1.08(2)
O3	x	−0.2592(1)	−0.2579(3)
	y	0.2201(1)	0.2229(3)
	z	0.0267(1)	0.0261(1)
	B_{iso} (Å^2)	0.95(1)	1.08(2)
Te	B_{iso} (Å^2)	0.81(3)	0.95(2)
Co/Mg	B_{iso} (Å^2)	0.81(3)	0.95(2)
a (Å)		5.6314(2)	5.6278(1)
b (Å)		5.5969(3)	5.5935(1)
c (Å)		7.9196(4)	7.9144(1)
β (°)		89.954(4)	89.952(4)
V (Å^3)		245.48(2)	249.14(1)
R_p (%)		4.46	5.20
R_{wp} (%)		5.81	6.81
R_{exp} (%)		2.74	2.80
χ^2		6.2	7.3
R_{Bragg}		4.44	5.59

ordering, is zero. Consequently, the structures consist of anti-ferromagnetically coupled layers along the c axis. In each layer the spins are ferromagnetically ordered, and located within the ac plane making an angle $\delta = 26(3)°$ with the c axis. The
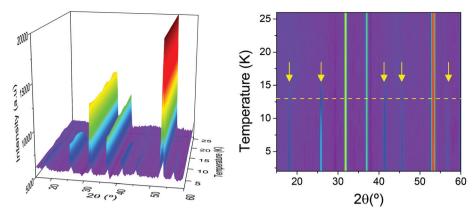
Fig. 13 Diffraction patterns collected on D1B as the temperature decreases for $Sr_2Co_{0.9}Mg_{0.1}TeO_6$. Emergence of magnetic reflections is marked by an arrow at T_N. Zoom of the low 2θ.
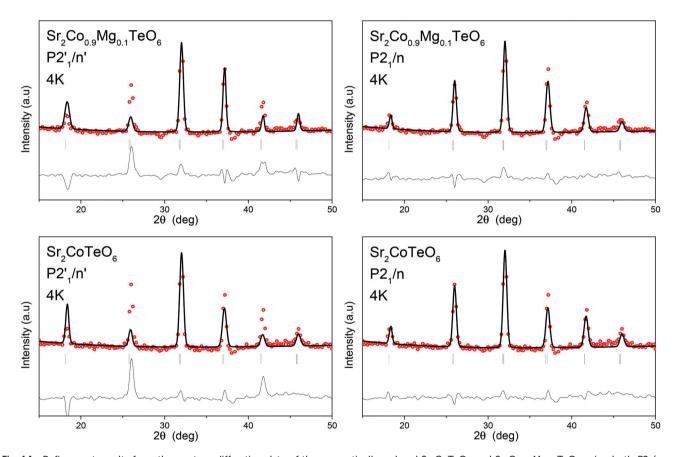

Fig. 14 Refinement results from the neutron diffraction data of the magnetically ordered Sr_2CoTeO_6 and $Sr_2Co_{0.9}Mg_{0.1}TeO_6$ using both $P2_1/n$ and $P2'_1/n'$ symmetries.

spin atom direction is not unambiguously solved: the refinements are equivalent for δ and $-\delta$ values, see Fig. 15.

Note that, if any canting is present in the structure, as predicted by magnetic measurements, it must occur along the y axis, since it is along this direction that a ferromagnetic coupling is allowed. At zero magnetic field this canting is not observed, probably because it is too small to be detected by neutron powder diffraction.

The expected value at low temperatures for the moments, calculated from the equation $\mu_{eff} = gS$, should be $\mu_{eff} \approx 3\mu_B$, with $S = 3/2$ and $g \approx g_e$. The obtained values are considerably deviated from the expected value. But taking into account that

Table 9 Refined parameters of the magnetic structures of Sr_2CoTeO_6 and $Sr_2Co_{0.9}Mg_{0.1}TeO_6$ at 4 K. Only the spin components of Co atoms in (0,0,1/2) are given. The data cannot distinguish Model 1 from Model 2

Co at (0,0,1/2)	Sr_2CoTeO_6	$Sr_2Co_{0.9}Mg_{0.1}TeO_6$
Model 1		
M_x	$0.93(7)\mu_B$	$0.84(8)\mu_B$
M_y	0	0
M_z	$1.88(5)\mu_B$	$1.77(5)\mu_B$
M	$2.10(9)\mu_B$	$1.96(9)\mu_B$
δ	$26(3)°$	$26(3)°$
Model 2		
M_x	$-0.93(7)\mu_B$	$-0.84(8)\mu_B$
M_y	0	0
M_z	$1.88(5)\mu_B$	$1.77(5)\mu_B$
M	$2.10(9)\mu_B$	$1.96(9)\mu_B$
δ	$-26(3)°$	$-26(3)°$
R_p/%	2.13	2.13
R_{wp}	3.06	3.12

the Co^{2+} ion, at low temperatures, changes to an effective spin value of $S' = 1/2$ and that $g \approx 4.3$, the theoretical value is $\mu_{eff} \approx 2.17\mu_B$. The experimental value $\mu_{eff} \approx 2.10(9)\mu_B$, and the ones from EPR, are in very good agreement with the theoretical value.

In the analysis we have done and in the way we are proposing the magnetic structure, we are making use of the total symmetry of the system, which takes into account the crystal and magnetic degrees of freedom. This results in some restrictions on the magnetic structure, imposed by the total symmetry of the system, and reveals some ambiguities, in the form of spurious degrees of freedom introduced *ad-hoc* in the course of the data treatment without taking into account the symmetry of the crystal. The only resulting arbitrariness in the present analysis comes from the fact that the data cannot distinguish between the model 1 and model 2 proposed.

4. Conclusions

This paper shows that the system $Sr_2Co_xMg_{1-x}TeO_6$ experiments structural changes both at room temperature (from $P2_1/n$ if $x \leq 0.1$ to $I2/m$ if $x \leq 0.5$ to $I4/m$ if $x \geq 0.5$) and at high temperature (with a similar sequence, that is: $P2_1/n \rightarrow I2/m \rightarrow I4/m \rightarrow Fm\bar{3}m$).

Regarding the amplitude values of the symmetry adapted modes taking part in the symmetry breaking from the prototype cubic symmetry to the low temperature distorted structures, the usual behavior of these kinds of materials with the ordered double perovskite structure has also been observed: not all the freedom allowed by symmetry is used by the system. Only three relevant modes GM_4^+, X_3^+ and X_5^+ in $P2_1/n$ (and essentially the first two, the order parameters), and only one, GM_4^+, in $I2/m$ and $I4/m$ contribute to the distorted structures observed experimentally. GM_4^+ in all the distorted structures represents essentially the same atomic displacement pattern, and consequently varies continuously with temperature until the distortion completely disappears in the prototype phase. As expected, we have shown that there is a correlation between the distortion degree at room-temperature and the temperature at which the distortion disappears: the bigger the distortion the higher is the interval in which the system is distorted, irrespective of the intermediate distorted phase; indeed, considering both. Besides, there is also a correlation between the intervals in which the second distorted structure is present: the transition temperature between both intermediate phases also increases with the distortion.

As the Mg doping increases there is a progressive diminution of the monoclinic distortion, and this points to an intermediate composition, $x \geq 0.5$, for which the monoclinic distortion disappears. At the time of writing this report, there is no experimentally found cubic symmetry structure for the compounds in the series.

The general conclusion regarding the set of amplitudes and the set of structures is the same: there is no appreciable differ-
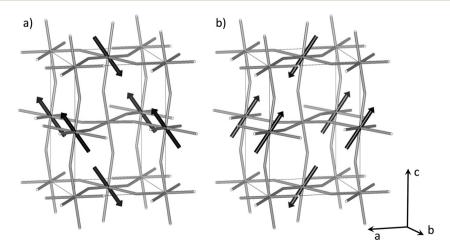

Fig. 15 Sketch of (a) Model 1 and (b) Model 2 for the magnetic structure of Sr_2CoTeO_6 and $Sr_2Co_{0.9}Mg_{0.1}TeO_6$ at 4 K.

ence between the model with all the freedom or with a (symmetry-guided-) restricted freedom. The fixed amplitudes left the atomic displacements related to the corresponding modes without effect, which indicates that the distortion with respect to the cubic prototype phase they represent is not effectively present.

At room-temperature, the mode-amplitudes *vs.* tolerance factor distinguish both monoclinic distortions in the symmetry change, and the octahedral tilt-angles in the centered phase are a little bit smaller than those in the primitive.

The finite jump in the amplitude values at the tetragonal-to-cubic phase transition could be attributed to the non-complete second order character of the transition. (This is often observed experimentally in these kinds of systems.) There are no appreciable jumps in the amplitude values of GM_4^+ at the crossing of the phase transitions down to the lowest temperatures.

Diffuse reflectance measurements have shown that the Co–O bond has a small degree of covalence and its properties at room temperature can be explained considering a high spin Co^{2+} (consistent with the magnetic properties). At low temperatures, EPR data confirm the change in the magnetic properties of cobalt which have to be described with an effective $S = 1/2$ and $g = 4.3$ that is also consistent with the neutron diffraction data.

The main magnetic interactions are antiferromagnetic and a spin–orbit coupling typical of the Co^{2+} in octahedral coordination. Replacing the Co^{2+} with Mg^{2+} weakens the antiferromagnetic interactions, both the Curie–Weiss temperature (θ) and the Néel temperature, T_N, decrease as Mg^{2+} increases, which indicates that Mg^{2+} replaces cobalt ions randomly and homogeneously in all compounds. The possible presence of inhomogeneities (Co-clusterization), suggested by EPR, is not present in these data. The small irreversibility in the ZFC and FC magnetic susceptibility curves is caused by a canting of the Co^{2+} spins; the spin glass-behavior is ruled-out due to its very small value (at 5 K the residual magnetization is about 0.08 emu mol^{-1}).

We have solved the magnetic structures for two compositions (the only ones for which we had NPD data at low temperature). In the analysis performed to propose the magnetic structure, we make use of the total symmetry of the system, taking into account the crystal and magnetic degrees of freedom. We have shown that the space group that describes the low temperature crystal and magnetic structures is the same: $P2_1/n$. This imposes an antiferromagnetic coupling for x- and z-spin components and a ferromagnetic coupling for the y-spin component between the cobalt atoms. Our data cannot distinguish between two possible models. This work constitutes another proof of the fact that the use of the total symmetry of the systems results directly in a non-arbitrary model for the magnetic structure.

Magnetically, the structures consist of antiferromagnetically coupled layers along the c axis, with the spins in the layer ferromagnetically ordered, located within the ac plane making an angle $\delta = 26(3)°$ with the c axis. The direction of the spin atoms is not unambiguously solved: the refinements are equivalent for δ and $-\delta$ values. The canting predicted by the magnetic measurements, if present, must occur along the y axis, since it is along this direction that a ferromagnetic coupling is allowed. At zero magnetic field no canting is observed (probably it is too small to be detected by neutron powder diffraction). The experimental value $\mu_{eff} \approx 2.10(9)\mu_B$ obtained at low temperature and those from EPR are in very good agreement with the theoretical value.

References

1 K.-I. Kobayashi, T. Kimura, H. Sawada, K. Terakura and Y. Tokura, *Nature*, 1998, **395**, 677–680.

2 A. J. Hauser, R. E. A. Williams, R. A. Ricciardo, A. Genc, M. Dixit, J. M. Lucy, P. M. Woodward, H. L. Fraser and F. Yang, *Phys. Rev. B: Condens. Matter*, 2011, **83**, 014407.

3 Y.-H. Huang, R. I. Dass, Z.-L. Xing and J. B. Goodenough, *Science*, 2006, **312**, 254–257.

4 M. Azuma, K. Takata, T. Saito, S. Ishiwata, Y. Shimakawa and M. Takano, *J. Am. Chem. Soc.*, 2005, **127**, 8889–8892.

5 N. S. Rogado, J. Li, A. W. Sleight and M. A. Subramanian, *Adv. Mater.*, 2005, **17**, 2225–2227.

6 Z. Xia, J. Sun, H. Du, D. Chen and J. Sun, *J. Mater. Sci.*, 2010, **45**, 1553–1559.

7 Z. Deng, J. Smit, H. Niu, G. Evans, M. Li, Z. Xu, J. Claridge and M. Rosseinsky, *Chem. Mater.*, 2009, **21**, 5154–5162.

8 A. Gómez-Pérez, M. Yuste, J. C. Pérez-Flores, C. Ritter, M. Teresa Azcondo, J. Canales-Vázquez, M. Gálvez-Sánchez, K. Boulahya, F. García-Alvarado and U. Amador, *J. Power Sources*, 2013, **227**, 309–317.

9 R. Mathieu, S. A. Ivanov, R. Tellgren and P. Nordblad, *Phys. Rev. B: Condens. Matter*, 2011, **83**, 174420.

10 S. A. Ivanov, P. Nordblad, R. Mathieu, R. Tellgren and C. Ritter, *Dalton Trans.*, 2010, **39**, 5490–5499.

11 L. Ortega-San Martín, J. P. Chapman, L. Lezama, J. Sanchez-Marcos, J. Rodriguez-Fernandez, M. I. Arriortua and T. Rojo, *J. Mater. Chem.*, 2005, **15**, 183–193.

12 S. A. Ivanov, P. Nordblad, R. Mathieu, R. Tellgren and C. Ritter, *Dalton Trans.*, 2010, **39**, 11136–11148.

13 B. Orayech, A. Faik, G. A. López, O. Fabelo and J. M. Igartua, *J. Appl. Crystallogr.*, 2015, **48**, 318–333.

14 A. Faik, E. Iturbe-Zabalo, I. Urcelay and J. M. Igartua, *J. Solid State Chem.*, 2009, **182**, 2656–2663.

15 A. Faik, J. M. Igartua, M. Gateshki and G. J. Cuello, *J. Solid State Chem.*, 2009, **182**, 1717–1725.

16 A. Faik, J. M. Igartua, E. Iturbe-Zabalo and G. J. Cuello, *J. Mol. Struct.*, 2010, **963**, 145–152.

17 A. Faik, I. Urcelay, E. Iturbe-Zabalo and J. M. Igartua, *J. Mol. Struct.*, 2010, **977**, 137–144.

18 H. M. Rietveld, *J. Appl. Crystallogr.*, 1969, **2**, 65–71.

19 V. Petricek, M. Dusek and L. Palatinus, *Z. Kristallogr.*, 2004, **229**, 345–352.

20 K. Momma and F. Izumi, *J. Appl. Crystallogr.*, 2008, **41**, 653–658.

21 C. J. Howard and H. T. Stokes, *Acta Crystallogr., Sect. B: Struct. Sci.*, 1998, **54**, 782–789.

22 T. Hahn, *International Tables for Crystallography Volume A Space-group symmetry*, The International Union of Crystallography and Kluwer Academic Publishers, Dordrecht, Holland, 1992.

23 R. Ubic, S. Letourneau, S. Thomas, G. Subodh and M. T. Sebastian, *Chem. Mater.*, 2010, **22**, 4572–4578.

24 D. Orobengoa, C. Capillas, M. I. Aroyo and J. M. Perez-Mato, *J. Appl. Crystallogr.*, 2009, **A42**, 820–833.

25 M. I. Aroyo, J. M. Perez-Mato, C. Capillas, E. Kroumova, S. Ivantchev, G. Madariaga, A. Kirov and H. Wondratsechek, *Z. Kristallogr.*, 2006, **221**, 15–27.

26 M. I. Aroyo, A. Kirov, C. Capillas, J. M. Perez-Mato and H. Wondratsechek, *Acta Crystallogr., Sect. A: Found. Crystallogr.*, 2006, **A62**, 115–128.

27 J. Rodríguez-Carvajal, *Physica B*, 1993, **192**, 55.

28 E. Iturbe-Zabalo, J. M. Igartua, A. Larrañaga, V. Pomjakushin, G. R. Castro and G. J. Cuello, *J. Phys.: Condens. Matter*, 2013, **25**, 205401.

29 E. Iturbe-Zabalo, A. Faik, A. Larrañaga, M. Hoelzel, G. Cuello and J. M. Igartua, *J. Solid State Chem.*, 2013, **198**, 24–38.

30 A. Faik, D. Orobengoa, E. Iturbe-Zabalo and J. Igartua, *J. Solid State Chem.*, 2012, **192**, 273–283.

31 R. B. Macquart, B. J. Kennedy and M. Avdeev, *J. Solid State Chem.*, 2010, **183**, 2400–2405.

32 J. M. Perez-Mato, D. Orobengoa and M. I. Aroyo, *Acta Crystallogr., Sect. A: Found. Crystallogr.*, 2010, **A6**, 558–590.

33 J. Zúñiga, J. M. Perez-Mato, D. Orobengoa, V. Petricek and T. Breczewski, *Z. Kristallogr.*, 2011, **226**, 454–466.

34 E. K. H. Salje, Phase Transitions in Ferroelastic and Co-elastic Crystals, in *Cambridge Topics in Mineral Physics and Chemistry*, Cambridge University Press, The Pitt Building, Trumpington Street, Cambridge CB2 1RP, 1990, vol. 1.

35 U. Petralanda and I. Etxebarria, *Phys. Rev. B: Condens. Matter*, 2014, **89**, 064107.

36 P. Atkins, T. Overton, J. Rourke, M. Weller, F. Armstrong, P. Salvador, M. Hagerman, T. Spiro and E. Stiefel, *Shriver and Atkins Inorganic Chemistry*, W.H. Freeman and Company, New York, 2006, 4th edn, pp. 478–483.

37 V. A. Koptsik, *Shubnikov Groups. Handbook on the Symmetry and Physical Properties of Crystal Structures*, translated by J. Kopecky, J. and Loopstra, B. O. Fysica Memo 175, Stichting, Reactor Centrum Nederlands, 1971.

38 C. J. Bradley and A. P. Cracknell, *The mathematical theory of symmetry in solids: representation theory for point groups and space groups*, Clarendon Press, Oxford, 1972.

39 J. Perez-Mato, S. Gallego, E. Tasci, L. Elcoro, G. d. l. Flor and M. Aroyo, *Annu. Rev. Mater. Res.*, 2015, **45**, 1–31.

40 B. Orayech, I. Urcelay-Olabarria, G. A. López, O. Fabelo, A. Faik and J. Mirena Igartua, *Dalton Trans.*, 2015, DOI: 10.1039/C5DT01532D.